Supplementary Information: Quantum electrodynamics of photonic time crystals

Junhyeon Bae[1,*], Kyungmin Lee[2,*], Bumki Min[2,†], Kun Woo Kim[1,‡]

[1]*Department of Physics, Chung-Ang University, 06974 Seoul, Republic of Korea*
[2]*Department of Physics, Korea Advanced Institute of Science and Technology, Daejeon 34141, Republic of Korea*
[*]*These authors contributed equally to this work.*
[†]*bmin@kaist.ac.kr*
[‡]*kunx@cau.ac.kr*

Supplementary Note 1. QUASI-EIGENENERGY SPECTRA OF $\hat{U}_F$, $\hat{H}_F$, AND $\hat{H}_F^{\text{eff}}$

The Hamiltonian of the quantum PTC is given by [1]:

$$\hat{H}(t) = \frac{k}{2}\left(1+\frac{1}{\varepsilon(t)}\right)\left(\hat{a}_k^\dagger \hat{a}_k + \hat{a}_{-k}^\dagger \hat{a}_{-k}\right) + \frac{k}{2}\left(1-\frac{1}{\varepsilon(t)}\right)\left(\hat{a}_k^\dagger \hat{a}_{-k}^\dagger + \hat{a}_k \hat{a}_{-k}\right), \tag{S1.1}$$

where $\varepsilon(t)$ is a periodic function with period T, i.e., $\varepsilon(t) = \varepsilon(t+T)$. The total momentum operator is $\hat{P} = k(\hat{n}_k - \hat{n}_{-k}) = k\delta\hat{n}_k$ and it commmutes with the Hamiltonian, $[\hat{H}(t), \hat{P}] = 0$. We can determine the energy spectrum of the Hamiltonian by introducing the Floquet operator $\hat{U}_F \equiv \hat{U}(T,0) = \mathcal{T}\exp\Big(-i\int_0^T \hat{H}(t)dt\Big)$, which governs the time evolution of a state for one period of time,

$$|\psi(T)\rangle = \hat{U}_F|\psi(0)\rangle. \tag{S1.2}$$

The Floquet operator can be numerically computed in the photon number basis by the discretization of time, then eigenstates and eigenvalues can be obtained, $\hat{U}_F\,|\psi_m\rangle = \exp\left(-iE_m^{\delta n_k}\,T\right)|\psi_m\rangle$, where m is eigenindex ($m = 0, 1, 2, \cdots$) in the increasing order of photon number expectation value, $\langle\hat{N}\rangle_{\psi_m} = \langle\psi_m|\,\hat{N}\,|\psi_m\rangle$.

In the main text we employ the Floquet Hamiltonian formalism, a framework particularly well-suited for analyzing periodically driven systems. This approach allows for a systematic calculation of quasi-eigenenergies by expressing the time-dependent Hamiltonian in terms of its Fourier components. The Floquet Hamiltonian $\hat{H}_F$ is defined through its matrix elements as:

$$(\hat{H}_F)_{l_F l'_F} = -l_F\Omega\,\hat{\delta}_{l_F l'_F} + \frac{1}{T}\int_0^T \hat{H}(t)\,e^{-i\Omega(l_F - l'_F)t}\,dt, \tag{S1.3}$$

where $\Omega = 2\pi/T$ is the driving frequency, and l_F, l'_F are the Floquet indices corresponding to the Fourier components of the time-periodic Hamiltonian $\hat{H}(t)$. To simplify the analysis near the critical momentum k_{c-}, where the eigenvalues coalesce into a single point (as shown in Supplementary Fig. 1a), $\hat{H}_F$ is reduced to an effective Hamiltonian $\hat{H}_F^{\text{eff}}$ by collecting states with the same onsite potential at $k = \Omega/2$ in the Floquet-photonic space. The reduction is performed in the basis $\{|n\rangle_{\delta n_k} \otimes |l_F{=}n\rangle\}$, where $|n\rangle_{\delta n_k} = |n_k{=}n + \delta n_k, n_{-k}{=}n\rangle$, $n = 0, 1, 2, \ldots$ denotes the photon occupation number with wave number $-k$, and l_F is the Floquet index. Note that without the loss of generality $l_F = n$ is chosen because Floquet spectrum of $l_F = n+1$ is identical up to a energy shift by $-\Omega$. The matrix elements of the effective (reduced) Floquet Hamiltonian carrying total momentum $P = \delta n_k k$ are expressed as:

$$(\hat{H}_F^{\text{eff}})_{n,n';\delta n_k} = -n\Omega\,\delta_{nn'} + \frac{1}{T}\int_0^T \langle n|\hat{H}(t)|n'\rangle_{\delta n_k}\,e^{-i\Omega(n-n')t}\,dt. \tag{S1.4}$$

For $\varepsilon^{-1}(t) = 1 - 2\alpha_c\cos(\Omega t)$, the reduced Floquet Hamiltonian takes the form:

$$\hat{H}_F^{\text{eff}} = \hat{H}_{\text{ph}} + \hat{H}_{\text{hopping}} + \hat{H}_{\text{Floquet}}, \tag{S1.5}$$

where the elements are defined as:

- The first diagonal term is from the counting of the number of photons:

$$(\hat{H}_{\text{ph}})_{n,n;\delta n_k} = k(2n + \delta n_k), \tag{S1.6}$$

- The second term is the Floquet hopping term between the nearest neighbor in the Floquet-photonic lattice:

$$(\hat{H}_{\text{hopping}})_{n,n+1;\delta n_k} = (\hat{H}_{\text{hopping}})_{n+1,n;\delta n_k} = \frac{k\alpha_c}{2}\sqrt{(n+\delta n_k+1)(n+1)}, \tag{S1.7}$$

- The third term is diagonal Floquet onsite energy:

$$(\hat{H}_{\text{Floquet}})_{n,n;\delta n_k} = -n\Omega. \tag{S1.8}$$

All other elements of the matrix are zero. By diagonalizing $\hat{H}_F^{\text{eff}}$, we obtain the quasi-eigenenergies, which are shown as solid lines in Supplementary Fig. 1a. The quasi-eigenenergies obtained from the diagonalization of $\hat{U}_F$ are plotted in the dashed lines. The two spectra are identical up to a momentum shift as shown in Supplementary Fig. 1b, demonstrating the robustness and reliability of the effective Hamiltonian approximation. This indicates that the effective Floquet Hamiltonian captures the essential physics near the critical point. The overall momentum shift between the two spectra can be analytically estimated within an arbitrary precision of α_c, see Supplementary Note 4.

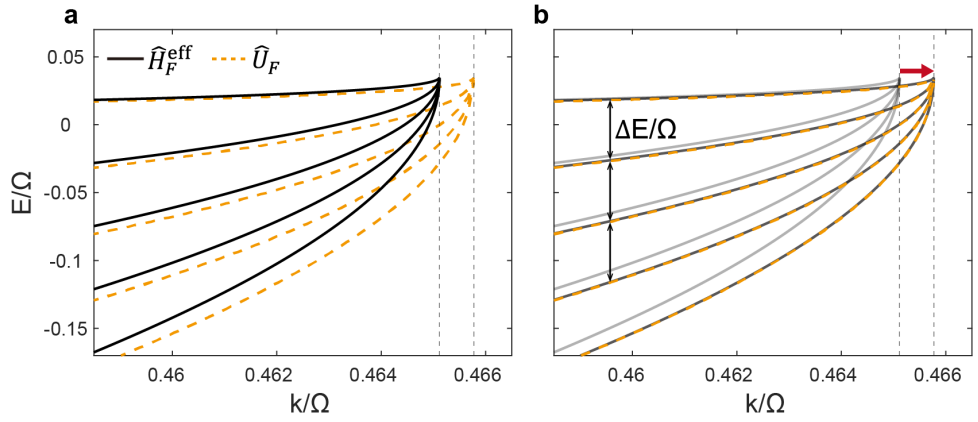

Supplementary Figure 1. (a) Quasi-eigenenergy spectrum of the quantum PTC as a function of the momentum k. Solid lines represent the quasi-eigenenergies obtained from the effective Floquet Hamiltonian $\hat{H}_F^{\text{eff}}$, while dashed lines indicate the quasi-eigenenergies derived directly from the Floquet evolution operator $\hat{U}_F$. The vertical dashed lines mark the momentum gap edges for two cases. (b) The spectrum calculated using $\hat{U}_F$ (dashed lines) and $\hat{H}_F^{\text{eff}}$ (solid lines) up to a momentum shift (see Supplementary Note 4), as highlighted by the arrows.

Importantly, from the spectrum of the quantum PTC, we can reconstruct the spectrum of the classical PTC. That is, the difference between eigenenergies, $\pm(E_m^{\delta n_k=1} - E_m^{\delta n_k=0}) + l_F\Omega$ restores the whole eigenfrequency spectrum of the classical PTC. Supplementary Figure 2a demonstrates that the spectrum of the positive slope is reproduced by $\omega_{\text{CPTC,+}} = +(E_m^{\delta n_k=1} - E_m^{\delta n_k=0})$ and the spectrum of the negative slope is reproduced by $\omega_{\text{CPTC,-}} = \Omega - (E_m^{\delta n_k=1} - E_m^{\delta n_k=0})$. Other Floquet side bands can be reproduced by choosing different l_F.

Next, when k approaches edges of the momentum gap, k_{c-}, the slope of the spectrum increases, accompanied by a divergence in the difference of the photon number expectation values, $\langle\hat{N}\rangle$ between $\delta n_k = 0$ and $\delta n_k = 1$. Supplementary Figure 2b illustrates the difference in photon number expectation values, $\langle\hat{N}\rangle$, between the eigenstates for $\delta n_k = 1$ and $\delta n_k = 0$, along with the corresponding probability distributions of these eigenstates in Supplementary Fig. 2c-e. For each δn_k, the eigenstate with the minimum $\langle\hat{N}\rangle$ is selected ($m = 0$). When $k/k_{c-} \ll 1$, the probability distributions for $\delta n_k = 0$ and $\delta n_k = 1$ are nearly identical (Supplementary Fig. 2c), resulting in the difference in $\langle\hat{N}\rangle$ remaining constant at approximately 1. However, as k/k_{c-} approaches 1, the distributions show significant deviations, leading to a larger difference in $\langle\hat{N}\rangle$ (Supplementary Fig. 2d-e). This explains the diverging difference of the average photon number shown in Supplementary Fig. 2b, $\langle\hat{N}^{\delta n_k=1}\rangle - \langle\hat{N}^{\delta n_k=0}\rangle$, and it indicates the amplitude of oscillation in the corresponding classical PTC diverges at the critical momentum as well. Note that this information is available only through the analysis of the quantum PTC.

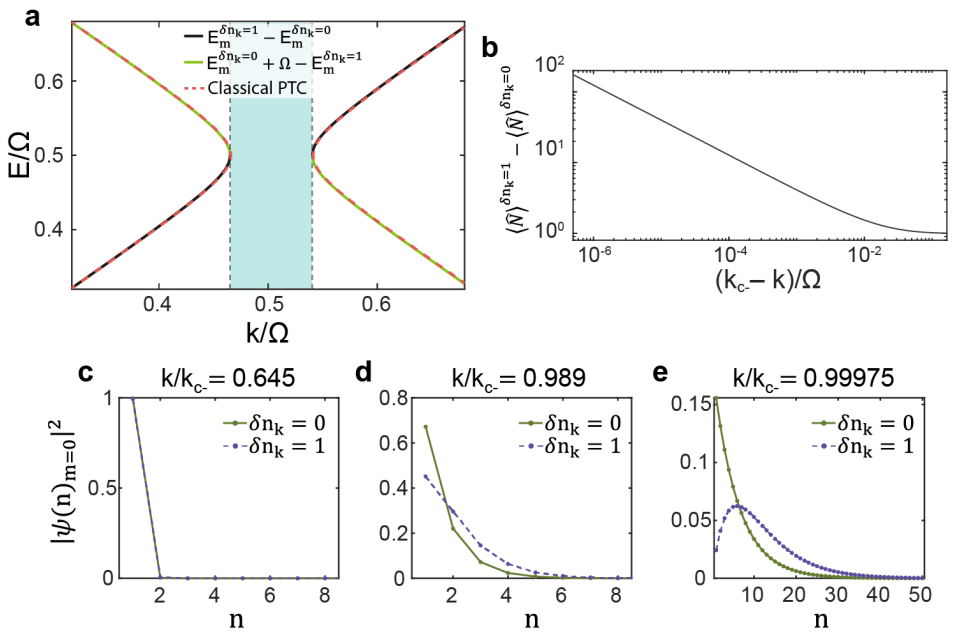

Supplementary Figure 2. (a) The energy spacing between eigenstates differed by one total momentum quanta precisely reproduces the spectrum of the classical PTC. (b) The difference in the expectation values of the photon number, $\langle\hat{N}\rangle$, between the eigenstates with $\delta n_k = 0$ and $\delta n_k = 1$. For each m, the eigenstate with the minimum $\langle\hat{N}\rangle$ is used ($m = 0$). As k approaches the edge of the momentum gap, k_{c-}, the difference in $\langle\hat{N}\rangle$ increases with $\langle\hat{N}\rangle^{\delta n_k=1} - \langle\hat{N}\rangle^{\delta n_k=0} \sim 1/|k_{c-} - k|^2$. (c-e) Probability distributions of the eigenstates $P(n) = |{}_{\delta n_k}\langle n|\psi_{m=0}\rangle|^2$ with the minimum $\langle\hat{N}\rangle$ for $\delta n_k = 0$ and $\delta n_k = 1$. For $k/k_{c-} \ll 1$, the probability distributions have nearly identical shapes, with a difference in $\langle\hat{N}\rangle$ of approximately 1. As k/k_{c-} approaches 1, the probability distributions become increasingly distinct, resulting in a larger difference in $\langle\hat{N}\rangle$.

Supplementary Note 2. TRANSFER MATRIX APPROACH FOR THE QUANTUM PTC

The effective Floquet Hamiltonian $\hat{H}_F^{\text{eff}}$ is given by:

$$\hat{H}_F^{\text{eff}} = \sum_{n=0}^{\infty} \left[(2n + \delta n_k)k - n\Omega\right] |n\rangle\langle n| + \frac{1}{2}k\alpha_c\sqrt{(n+1)(n+\delta n_k+1)}\left[|n\rangle\langle n+1| + h.c.\right], \tag{S2.1}$$

which provides an effective description of the quantum PTC in the vicinity of the critical momentum. The difficulty dealing with the Hamiltonian from a direct diagonalization is that the coefficients of *onsite* and *hopping* terms grows indefinitely as $n \to \infty$, implying that near the critical momentum and within the momentum gap the finite size effect is uncontrolled. The transfer matrix offers an alternative route by focusing on the relation of neighboring amplitudes of wave functions. The recursive relation of $\psi(n) = \langle n|\psi\rangle$ can be obtained from $\langle n|\,\hat{H}_F^{\text{eff}}\,|\psi\rangle = E\langle n|\psi\rangle$,

$$E\psi(n) = [(2n + \delta n_k)k - n\Omega]\psi(n) + \frac{1}{2}k\alpha_c\sqrt{(n+1)(n+\delta n_k+1)}\psi(n+1) + \frac{1}{2}k\alpha_c\sqrt{n(n+\delta n_k)}\psi(n-1). \tag{S2.2}$$

The transfer matrix connects the neighboring amplitudes of wave function:

$$\begin{bmatrix}\psi(n+1)\\ \psi(n)\end{bmatrix} = T_n\begin{bmatrix}\psi(n)\\ \psi(n-1)\end{bmatrix} = T_n\Psi(n-1), \tag{S2.3}$$

where the transfer matrix T_n is

$$T_n = \begin{bmatrix} \frac{2}{\alpha_c k}\frac{(E+n(\Omega-2k)-k\delta n_k)}{(n+1)\sqrt{1+\delta n_k/(n+1)}} & -\frac{n\sqrt{1+\delta n_k/n}}{(n+1)\sqrt{1+\delta n_k/(n+1)}} \\ 1 & 0 \end{bmatrix}. \tag{S2.4}$$

For a given momentum k and energy E, the transfer matrix allows us to generate $\psi(n)$ from $\psi(n=0)$. As a result, the method is critically used for the accurate estimation of the Lyapunov exponent near the quantum phase transition to characterize universality classes [2–9]. The transfer matrix, while initially appearing complex, undergoes significant simplification in the limit as $n \to \infty$. The asymptotic form of the transfer matrix is:

$$\lim_{n\to\infty} T_n = T = \begin{bmatrix} \frac{2}{\alpha_c}\left(\frac{\Omega}{k}-2\right) & -1 \\ 1 & 0 \end{bmatrix} = \begin{bmatrix} Z & -1 \\ 1 & 0 \end{bmatrix}, \tag{S2.5}$$

where $Z = \frac{2}{\alpha_c}\left(\frac{\Omega}{k}-2\right)$. This expression highlights that, in the limit as $n \to \infty$, the transfer matrix becomes independent of both the energy and total momentum δn_k. The physical reason of taking this limit $n \to \infty$ is from the anticipation that when the eigenstates of the quantum PTC is delocalized in the Floquet-photonic space, the quantum dynamics taking place at larger n region is more important and eventually dominant as the strength of hopping is greater. This expectation is confirmed by matching our analytical prediction and numerical results.

In the classical PTC, the in-gap states lead to significant light amplification, while in the quantum PTC, this amplification manifests as the delocalization of the photon wave function across the Floquet-photonic lattice. We employ the transfer matrix to rigorously define the exact critical momentum at which the localization-delocalization transition occurs in the quantum PTC, thereby introducing the concept and demonstrating the analytical method for studying this transition.

The Lyapunov exponent in terms of the transfer matrix is defined as:

$$\gamma = \lim_{N\to\infty}\frac{1}{N}\ln\left[\frac{|\Psi(N)|}{|\Psi(0)|}\right] = \lim_{N\to\infty}\frac{1}{2N}\ln\left[\frac{\Psi^\dagger(0)T_1^\dagger T_2^\dagger T_3^\dagger\cdots T_N^\dagger T_N\cdots T_3T_2T_1\Psi(0)}{\Psi^\dagger(0)\Psi(0)}\right]. \tag{S2.6}$$

where $|\Psi(n)| = \sqrt{|\psi(n+1)|^2+|\psi(n)|^2}$. If the wave function is localized, the Lyapunov exponent γ is nonzero and positive; in contrast, a zero Lyapunov exponent signifies delocalization, defining the region known as the metallic phase. To simplify the computation, the transfer matrix sequence can be truncated at an intermediate point q, where $0 < q < N$ and $\Psi^\dagger(q)\Psi(q) \neq 0, \infty$. In this case, the Lyapunov exponent is equivalently expressed as:

$$\begin{aligned}\gamma &= \lim_{N\to\infty}\frac{1}{2N}\ln\left[\frac{\Psi^\dagger(q)T_{q+1}^\dagger T_{q+2}^\dagger\cdots T_N^\dagger T_N\cdots T_{q+2}T_{q+1}\Psi(q)}{\Psi^\dagger(q)\Psi(q)}\frac{\Psi^\dagger(q)\Psi(q)}{\Psi^\dagger(0)\Psi(0)}\right] \\ &= \lim_{N\to\infty}\frac{1}{2N}\ln\left[\frac{\Psi^\dagger(q)T_{q+1}^\dagger T_{q+2}^\dagger\cdots T_N^\dagger T_N\cdots T_{q+2}T_{q+1}\Psi(q)}{\Psi^\dagger(q)\Psi(q)}\right],\end{aligned} \tag{S2.7}$$

where $\Psi(q) = T_qT_{q-1}T_{q-2}\cdots T_1\Psi(0)$. Under the condition that $\Psi^\dagger(q)\Psi(q) \neq 0, \infty$, the term $\left[\Psi^\dagger(q)\Psi(q)/\Psi^\dagger(0)\Psi(0)\right]$ can be factored out as an additive constant outside the logarithm. As $N \to \infty$, q remains finite, causing the separated term to vanish in the limit and leaving the Lyapunov exponent unaffected. Thus, the starting point of the calculation does not affect the determination of the critical point or the critical exponent. Now, we select q to be sufficiently large so that the transfer matrix converges to its asymptotic form, as given in Eq. (S2.5). This allows us to express the Lyapunov exponent as

$$\gamma \approx \lim_{N\to\infty}\frac{1}{2N}\ln\left[\frac{\Psi^\dagger(q)(T^\dagger T)^{N-q}\Psi(q)}{\Psi^\dagger(q)\Psi(q)}\right]. \tag{S2.8}$$

The Lyapunov exponent can be expressed solely using Eq. (S2.5), indicating that the critical point and the critical exponent depend only on the momentum k and the modulation parameters α_c, Ω. The eigenvalue equation of the transfer matrix is given by:

$$T\phi_\pm = \lambda_\pm\phi_\pm, \qquad \lambda_\pm = \frac{Z\pm\sqrt{Z^2-4}}{2}. \tag{S2.9}$$

Due to probability conservation, the transfer matrix is a symplectic matrix, meaning its eigenvalues satisfy the condition:

$\lambda_+\lambda_- = 1$. The q-th wave function can be decomposed into the eigenbasis of the transfer matrix as $\Psi(q) = C_+\phi_+ + C_-\phi_-$ where $\phi_\pm$ are not orthogonal and $C_\pm \neq 0$, in general. By plugging in, the Lyapunov exponent is given by:

$$\gamma = \lim_{N\to\infty} \frac{1}{2N} \ln\left[\frac{|\lambda_+^{N-q}C_+|^2 + (\lambda_+^*\lambda_-)^{N-q}C_+^*C_-\phi_+^\dagger\phi_- + (\lambda_+\lambda_-^*)^{N-q}C_+C_-^*\phi_+\phi_-^\dagger + |\lambda_-^{N-q}C_-|^2}{|C_+|^2 + C_+^*C_-\phi_+^\dagger\phi_- + C_+C_-^*\phi_+\phi_-^\dagger + |C_-|^2}\right]. \tag{S2.10}$$

When $Z^2 > 4$, the eigenvalues $\lambda_\pm$ are both real and separated by a square-root term. To capture the dominant contribution, we define $\lambda \equiv \max\big(|\lambda_+|, |\lambda_-|\big)$. The Lyapunov exponent γ is then governed by λ because, as $N \to \infty$, λ^{2N} dominates the exponential growth of the wave function norm in the Floquet-photonic space. Hence, we find that $\gamma = \ln(\lambda)$, which quantifies the rate of exponential localization. On the other hand, when $Z^2 \leq 4$, the eigenvalues lie on the unit circle (pure phase rotations), so $\gamma = 0$. To summarize, the Lyapunov exponent is

$$\gamma = \begin{cases} 0, & Z^2 \leq 4, \\ \ln\lambda = \ln\left[|\frac{Z}{2}| + \sqrt{\left(\frac{Z}{2}\right)^2 - 1}\right] = \operatorname{arcosh}(|\frac{Z}{2}|), & Z^2 > 4. \end{cases}$$

Because $|\psi(n)| \simeq e^{-\gamma n}|\psi(0)|$ for $n \gg 1$, $\gamma = 0$ corresponds to a delocalized phase, while $\gamma > 0$ corresponds to a localized phase. The phase transition between the two occurs at the critical momentum, and it is determined by the condition $Z^2 = 4$. Solving this yields

$$k_{c-} = \frac{\Omega}{2+\alpha_c}, \quad k_{c+} = \frac{\Omega}{2-\alpha_c}. \tag{S2.11}$$

Meanwhile, the localization length ξ is defined as the inverse of the Lyapunov exponent γ. Specifically,

$$\xi^{-1} = \gamma = \operatorname{arcosh}\left(\left|\frac{1-\Omega/2k}{1-\Omega/2k_{c\pm}}\right|\right), \quad k < k_{c-} \text{ or } k > k_{c+}. \tag{S2.12}$$

Equation (S2.12) expresses the localization length as a function of momentum. It shows that ξ diverges as k approaches k_{c-} from below ($k \to k_{c-} + 0^-$) and also as k approaches k_{c+} from above ($k \to k_{c+} + 0^+$). The following equation defines the critical exponent ν, which characterizes how the localization length ξ diverges near the critical point.

$$\nu = -\lim_{\delta\to 0} \frac{\ln\xi}{\ln\delta}, \quad \delta \equiv \left|\frac{k_{c\pm} - k}{k_{c\pm}}\right|. \tag{S2.13}$$

To analyze the behavior of ξ near $\lambda = 1$ (or $\gamma = 0$), we consider a Taylor expansion of $x\xi$ in terms of $x \equiv \lambda - 1$. Dividing out the leading factor x yields

$$\xi = \frac{1}{\ln\lambda} = \frac{1}{\ln(1+x)} = \frac{1}{x} + \frac{1}{2} + \ldots, \quad (x \equiv \lambda - 1). \tag{S2.14}$$

Now, focus on the regime $k < k_{c-}$ near the critical point. By examining how x scales with $\delta \equiv |\frac{k_{c-}-k}{k_{c-}}|$, one obtains

$$x = \delta\left[C(\Omega, k_{c-})\frac{1}{1-\delta} + \frac{1}{\sqrt{\delta}}\sqrt{C(\Omega, k_{c-})\frac{1}{1-\delta}\left(\frac{Z}{2}+1\right)}\right], \tag{S2.15}$$

where $C(\Omega, k_{c-})$ is a non-singular function. Because the highest power of δ in this expression is δ^1, the critical exponent ν follows as

$$\nu = -\lim_{\delta\to 0}\frac{\ln\xi}{\ln\delta} = \lim_{\delta\to 0}\frac{\ln x}{\ln\delta} = 1. \tag{S2.16}$$

Next, we establish the exponential growth of photonic energy within the momentum gap. The *classical* field growth rate γ_{cl} within the momentum gap of PTCs can be calculated from the imaginary part of the eigenfrequencies. Correspondingly, the photonic energy growth rate is $2\gamma_{\text{cl}}$. Here we proceed to derive the quantum counterpart of this result. In the analysis above, we focused on the localized regime as k approaches the critical point. At $k = k_{c\pm}$, the eigenvalues of the transfer matrix coalesce at $\lambda_\pm = 1$. Once the momentum enters the gap ($k \in \mathcal{K}_{\text{gap}}$), the eigenvalues can be written as $\lambda = e^{\mp i\phi}$, where $\phi = \pm\arccos\big(Z/2\big)$ and $Z = e^{i\phi} + e^{-i\phi}$. Under these conditions, the asymptotic transfer matrix from Eq. (S2.5) admits two

eigenvectors, $\frac{1}{\sqrt{2}}\left[e^{i\phi}\ 1\right]^T$ and $\frac{1}{\sqrt{2}}\left[e^{-i\phi}\ 1\right]^T$. Each state satisfies $\psi_t(n+1) = e^{\pm i\phi}\,\psi_t(n)$, indicating a freely propagating wave whose phase rotates uniformly from site n to site $n+1$. This phase progression sustains a net current within the Floquet–photonic lattice, ultimately causing the photonic energy to grow continuously. We define the photonic energy operator in the photon-number basis as $\hat{H}_{\text{ph}} = \text{diag}(0, 2k, 4k, \cdots) = k\hat{N}$, under the assumption $\delta n_k = 0$. Its expectation value evolves according to $d\langle\hat{H}_{\text{ph}}\rangle/dt = -i\langle\psi_t|\left[\hat{H}_F^{\text{eff}}, \hat{H}_{\text{ph}}\right]|\psi_t\rangle = \Sigma_n 2(n+1)\alpha_c k^2 \Im\left[\psi_t^*(n)\psi_t(n+1)\right]$. This shows that phase rotations across the photon-number basis directly produce the photonic energy current. By analogy with classical PTCs, the quantum exponential growth rate emerges as

$$\frac{1}{\langle\hat{H}_{\text{ph}}\rangle}\frac{d\langle\hat{H}_{\text{ph}}\rangle}{dt} = \frac{\sum_n 2(n+1)\alpha_c k^2 \Im\left[\psi_t^*(n)\psi_t(n+1)\right]}{\sum_n 2nk\left[\psi_t^*(n)\psi_t(n)\right]} \simeq \pm\frac{\sum_n 2(n+1)\alpha_c k^2 \sin\phi\left[\psi_t^*(n)\psi_t(n)\right]}{\sum_n 2nk\left[\psi_t^*(n)\psi_t(n)\right]} \simeq \pm\alpha_c k\sin\phi, \quad \text{(S2.17)}$$

which establishes the quantum analog of exponential photonic-energy growth observed in classical PTCs. Expressing ϕ in terms of momentum yields:

$$\gamma_{\text{qu}} = \pm\alpha_c k\sin\phi = \pm\alpha_c k\sqrt{1-\left(\frac{1-\Omega/2k}{1-\Omega/2k_{c-}}\right)^2} = \pm 2k\sqrt{\left(\frac{\Omega}{2k_{c-}}-1\right)^2 - \left(\frac{\Omega}{2k}-1\right)^2}. \quad \text{(S2.18)}$$

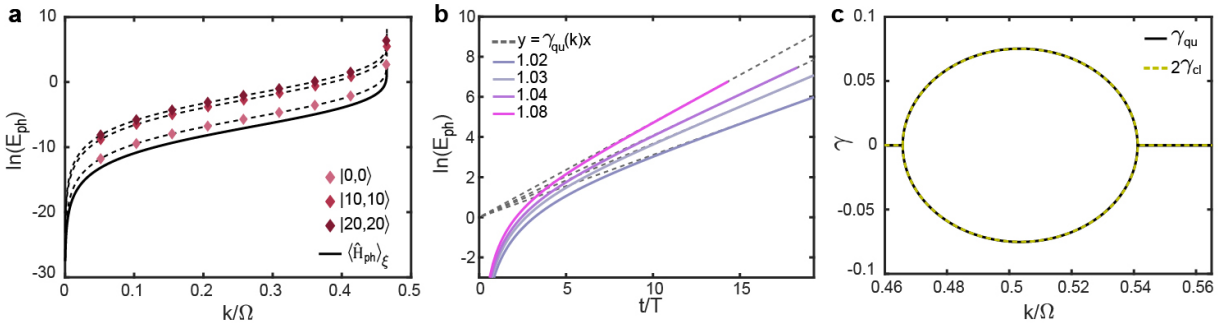

Supplementary Figure 3. (a) Relation between the localization length and photonic energy oscillation amplitude in localized regime $k \in \mathcal{K}_{\text{band}}$, Fig.3b in the main text. The states in the legend means the initial position of the wave function in 1-dimensional Floquet-photonic lattice $\{|n, n; l_F = n\rangle\}$ with $\delta n_k = 0$. $\langle\hat{H}_{\text{ph}}\rangle_\xi$ is photonic energy expectation value from the ansatz $|\psi_\xi(n)| \sim e^{-n/\xi}$. The data points (diamond marks) are the difference between maximum value and minimum value of the photonic energy oscillation, which is twice of oscillation amplitude. (b) Relation between the γ_{qu} and exponential growing rate in Fig.3c, in $k \in \mathcal{K}_{\text{gap}}$. The colored lines represent the $\ln(E_{\text{ph}}(t))$ shifted along the y-axis at momentum indicated in the legend: $k = 1.02k_{c-}, 1.03k_{c-}, 1.04k_{c-}, 1.08k_{c-}$. An initial ($t = 0$) quantum state is placed at $|0, 0; l_F = 0\rangle$. (c) Relation between the γ_{qu} and $2\gamma_{\text{cl}}$. The γ_{qu} is shifted along the x-axis due to the overall momentum shift between the classical PTC and $\hat{H}_F^{\text{eff}}$ (Supplementary Note 1, Supplementary Note 4). The numerical simulations are conducted with the condition of $\alpha_c = 0.15$.

In the localized regime, a wave packet initially placed at $|n, n;\ l_F = n\rangle$ undergoes oscillatory motion in the Floquet–photonic space, driven purely by phase interference among the $\hat{H}_F^{\text{eff}}$ eigenstates (see Fig.3b). The oscillation frequency of the photonic energy matches the uniform energy spacing of the quasi-eigenenergy spectrum (see Supplementary Note 6 for details). Moreover, the oscillation amplitude is directly tied to the wave-packet spread in the Floquet–photonic space, which is quantified by the localization length. By adopting the ansatz $|\psi_\xi(n)| = Ae^{-n/\xi}$ where $A = \sqrt{1-e^{-2/\xi}}$, the photonic energy expectation value $\langle\hat{H}_{\text{ph}}\rangle_\xi = \langle\psi_\xi|\hat{H}_{\text{ph}}|\psi_\xi\rangle$, is proportional to the oscillation amplitude as shown in Supplementary Fig. 3a. In the log-scale plot, the oscillation amplitude parallels $\langle\hat{H}_{\text{ph}}\rangle_\xi$ up to a constant vertical shift, demonstrated across three distinct initial wave-packet positions.

In the momentum-gap region $k \in \mathcal{K}_{\text{gap}}$, the wave function delocalizes over the Floquet–photonic basis, causing the photonic energy to grow exponentially (see Fig.3c). The growth rate of this energy directly reflects the phase-rotation rate (Eq. (S2.17)). Supplementary Figure 3b demonstrates excellent agreement between our analytic prediction and the numerical results obtained by evolving a wave packet initially at $|0, 0;\ l_F = 0\rangle$. Equation (S2.17) remains valid for $n \gg 1$, and the plot shows strong convergence of the numerical data at later times ($t/T > 10$). Lastly, Supplementary Fig. 3c demonstrates that γ_{qu} which we analytically computed above makes an excellent matching with the imaginary part of eigenfrequencies γ_{cl} with the extra factor of two. It is because the energy of electromagnetic waves in the classical PTC is $E_{\text{ph}}^{\text{classic}}(t) \sim e^{2\gamma_{\text{cl}}t}$. Without any introduction of non-Hermitian components, the behavior of exponentially growing field strength within the momentum gap is explained in the

quantum PTC by computing the photonic energy current when eigenstates are delocalized in the Floquet-photonic space.

Supplementary Note 3. TRANSFER MATRIX APPROACH FOR THE CLASSICAL PTC

In a PTC, Maxwell's equations dictate how the electromagnetic fields respond to time-varying permittivity. When the permittivity $\varepsilon(t)$ varies with time, these equations take the form

$$\nabla \times \mathbf{E} \,=\, -\,\frac{\partial \mathbf{B}}{\partial t}, \quad \nabla \times \mathbf{B} \,=\, \frac{\partial}{\partial t}\big[\varepsilon(t)\,\mathbf{E}\big], \tag{S3.1}$$

thereby illustrating the direct influence of temporal modulations in ε on $\mathbf{E}$ and $\mathbf{B}$. For simplicity, we assume a plane wave traveling along the x direction. In this configuration, the electric field oscillates along the y axis, while the magnetic field oscillates along the z axis. We then obtain a differential equation for the out-of-plane magnetic field B_z [10], which can be recast in a Schrödinger-like form:

$$k^2 B_z \,=\, \frac{\partial}{\partial t}\Big[\varepsilon\,\frac{\partial B_z}{\partial t}\Big], \qquad i\,\frac{\partial}{\partial t}\begin{bmatrix} B_z \\ \varepsilon\,\dot{B}_z \end{bmatrix} \,=\, \begin{bmatrix} 0 & i\,\varepsilon^{-1} \\ -\,i\,k^2 & 0 \end{bmatrix}\begin{bmatrix} B_z \\ \varepsilon\,\dot{B}_z \end{bmatrix} \,=\, \hat{H}_{\text{eff}}\begin{bmatrix} B_z \\ \varepsilon\,\dot{B}_z \end{bmatrix}. \tag{S3.2}$$

The resulting effective Hamiltonian is both non-Hermitian and time periodic, making it amenable to Floquet theory. In particular, we apply the transform indicated in Eq.(3) to recast the system into a higher-dimensional representation. We assume a single-frequency modulation of the inverse permittivity, $\varepsilon^{-1}(t) \,=\, 1 \,-\, 2\alpha_c \cos(\Omega t)$. This periodic function $\varepsilon(t)$ induces a Floquet Hamiltonian of the form

$$\begin{aligned} \tilde{H}_F(k) &= \sum_{n=-\infty}^{\infty} \begin{pmatrix} -n\Omega & i \\ -ik^2 & -n\Omega \end{pmatrix} |n\rangle\langle n| + \begin{pmatrix} 0 & -\,i\,\alpha_c \\ 0 & 0 \end{pmatrix} |n\rangle\langle n+1| + \begin{pmatrix} 0 & -\,i\,\alpha_c \\ 0 & 0 \end{pmatrix} |n+1\rangle\langle n|, \\ &= \sum_{n=-\infty}^{\infty} M_n\,|n\rangle\langle n| \;+\; J\,|n\rangle\langle n+1| \;+\; J\,|n+1\rangle\langle n|. \end{aligned}$$

Note that n is Floquet index only in contrast to the case of the quantum PTC where the photon number state $|n_k, n_{-k}\rangle$ is present in addition to the Floquet index l_F. The hopping matrix J is non-invertible and nilpotent, satisfying $J^2 = 0$ and $\det(J) = 0$. Consequently, the generalized transfer matrix method [6] needs to be employed. We choose the singular value decomposition of J as $J = V\Xi W^\dagger = [0\ -i]^T\,\alpha\,[0\ \ 1]$, where V and W span $\mathbb{C}^2$ as an orthonormal basis. From this construction, one obtains the following transfer-matrix relation:

$$\begin{bmatrix} W^\dagger\psi(n+1) \\ W^\dagger\psi(n) \end{bmatrix} = T_n \begin{bmatrix} W^\dagger\psi(n) \\ W^\dagger\psi(n-1) \end{bmatrix} = \begin{bmatrix} \frac{1}{\alpha}\left[1 - \left(\frac{E-n\Omega}{k}\right)^2\right] & -1 \\ 1 & 0 \end{bmatrix} \begin{bmatrix} \varepsilon\dot{B}_z(n) \\ \varepsilon\dot{B}_z(n-1) \end{bmatrix}. \tag{S3.3}$$

By diagonalizing, one can verify that the eigenvalues of $\tilde{H}_F$ are real and distinct within the band $k \in \mathcal{K}_{\text{band}}$. Inside the momentum gap $k \in \mathcal{K}_{\text{gap}}$, the eigenvalues remain complex-conjugate pairs, each acquiring an imaginary part that induces exponential growth or decay. At the momentum gap edge, these eigenvalues coalesce into a single value, marking an exceptional point of classical PTCs. At the gap edge, two distinct Floquet states merge into a single wave function for each Floquet index, rendering all eigenstates at this exceptional point symmetric across the Floquet indices. This symmetry implies that the transfer matrix acquires a unit eigenvalue when multiplied over a symmetric pair. For instance, consider the momentum gap around $E/\Omega = \frac{1}{2}$. Here, the product T_1T_0 couples the states $W^\dagger\psi(0)$, $W^\dagger\psi(-1)$ with $W^\dagger\psi(2)$, $W^\dagger\psi(1)$. That is,

$$\begin{bmatrix} W^\dagger\psi(2) \\ W^\dagger\psi(1) \end{bmatrix} = T_1T_0 \begin{bmatrix} W^\dagger\psi(0) \\ W^\dagger\psi(-1) \end{bmatrix}. \tag{S3.4}$$

At the critical momentum, $\psi(2)$ and $\psi(-1)$, as well as $\psi(1)$ and $\psi(0)$, share the same norm. Owing to this symmetric structure, the wave number associated with the unity eigenvalue denotes the transition. Extending the approach by computing $T_2T_1T_0T_{-1}$ yields a more precise estimate of the critical point. In this case, the analytic expression for the first-order momentum-gap edge is

$$k_{c-} \approx \frac{\Omega}{2 + \alpha_c - \frac{1}{8}\alpha_c^2 - \frac{5}{64}\alpha_c^3}, \tag{S3.5}$$

and can be further improved by including higher-order products of the transfer matrix.

The position of the momentum gap edge in a classical PTC described by $\varepsilon = \varepsilon_0 + \varepsilon_r \cos(\Omega t)$ has been analyzed in Ref. [10]. In the regime where $\left|\varepsilon_r/\varepsilon_0\right| \ll 1$ and $\varepsilon_0 = 1$, one obtains the approximate expression $k_- = \Omega(2-\varepsilon_r)/(4-\varepsilon_r)$. Ignoring the second order and higher in the analysis, $\tilde{H}_{n\geq 2} = 0$, the k_- is actually a perturbative estimation for $\varepsilon(t) = \varepsilon_0/(1-\frac{\varepsilon_r}{\varepsilon_0}\cos\Omega t)$. To compare with our result from the transfer matrix, let us Taylor expand the inverse of k_-:

$$k_-^{-1} = \frac{1}{\Omega}\left(\frac{4-\epsilon_r}{2-\epsilon_r}\right) \simeq \frac{1}{\Omega}\left(2 + \frac{\epsilon_r}{2} + \frac{\epsilon_r^2}{4} + O(\epsilon_r^3)\right), \tag{S3.6}$$

which is consistent with k_{c-}^{-1} up to the first order when we identify $\alpha_c = \epsilon_r/2$, but the second order correction deviates. Our derivation of Eq. (S3.5) relies on the symmetric structure of eigenvectors in the Floquet space and it provides more accurate results. The precision can be further enhanced by multiplying more transfer matrices, see Supplementary Note 4.

To extend the analysis, one can introduce a second harmonic in the inverse permittivity, $\varepsilon^{-1} = 1 - 2\alpha_c\cos(\Omega t) - 2\beta_c\cos(2\Omega t)$, where β_c generates an additional hopping term in the Floquet Hamiltonian. Building on this extension, the Floquet Hamiltonian takes the form

$$\begin{aligned}
\tilde{H}_F(k) = &\sum_{n=-\infty}^{\infty} \begin{pmatrix} -n\Omega & i \\ -ik^2 & -n\Omega \end{pmatrix} |n\rangle\langle n| + \begin{pmatrix} 0 & -i\alpha_c \\ 0 & 0 \end{pmatrix} |n\rangle\langle n+1| + \begin{pmatrix} 0 & -i\alpha_c \\ 0 & 0 \end{pmatrix} |n+1\rangle\langle n| \qquad \text{(S3.7)} \\
&+ \begin{pmatrix} 0 & -i\beta_c \\ 0 & 0 \end{pmatrix} |n\rangle\langle n+2| + \begin{pmatrix} 0 & -i\beta_c \\ 0 & 0 \end{pmatrix} |n+2\rangle\langle n|, \\
= &\sum_{n'=-\infty}^{\infty} \begin{pmatrix} -n\Omega & i & 0 & -i\alpha_c \\ -ik^2 & -n\Omega & 0 & 0 \\ 0 & 0 & -(n+1)\Omega & i \\ -i\alpha_c & 0 & -ik^2 & -(n+1)\Omega \end{pmatrix} |n'\rangle\langle n'| + \begin{pmatrix} 0 & -i\beta_c & 0 & 0 \\ 0 & 0 & 0 & 0 \\ 0 & -i\alpha_c & 0 & -i\beta_c \\ 0 & 0 & 0 & 0 \end{pmatrix} |n'\rangle\langle n'+1| \qquad \text{(S3.8)} \\
&+ \begin{pmatrix} 0 & -i\beta_c & 0 & -i\alpha_c \\ 0 & 0 & 0 & 0 \\ 0 & 0 & 0 & -i\beta_c \\ 0 & 0 & 0 & 0 \end{pmatrix} |n'+1\rangle\langle n'|, \\
= &\sum_{n'=-\infty}^{\infty} M_{n'}|n'\rangle\langle n'| + J_p|n'\rangle\langle n'+1| + J_m|n'+1\rangle\langle n'|, \qquad \text{(S3.9)}
\end{aligned}$$

where the enlarged unit cell is introduced that $|n'\rangle$ includes both $|n\rangle$ and $|n+1\rangle$. By extending the basis to include both the original set of states and an offset copy, we obtain a block-structured Hamiltonian that can be treated with the transfer matrix method. The resulting hopping matrices J_p and J_m are nilpotent, with $\det(J_p) = \det(J_m) = 0$ and $J_pJ_p = J_mJ_m = 0$. Consequently, their singular value decompositions, $J_p = V_p\Xi W_p^\dagger$, $J_m = V_m\Xi W_m^\dagger$, satisfy $V_p^\dagger W_p = V_m^\dagger W_m = 0$ and $V_p^\dagger V_p = V_m^\dagger V_m = W_p^\dagger W_p = W_m^\dagger W_m = \mathbb{1}$. Defining

$$\lambda_\pm = \beta_c^2 + \frac{\alpha_c^2}{2} + \sqrt{\alpha_c^2\beta_c^2 + \frac{\alpha_c^4}{4}}, \qquad f = \frac{\lambda_+ - \beta_c^2}{\alpha_c\beta_c} = \frac{\alpha_c}{2\beta_c} + \sqrt{1 + \frac{\alpha_c^2}{4\beta_c^2}}, \tag{S3.10}$$

one obtains $\Xi = \mathrm{diag}(\sqrt{\lambda_+}, \sqrt{\lambda_-})$ and

$$V_p = \frac{1}{\sqrt{1+f^2}}\begin{pmatrix} 1 & -f \\ 0 & 0 \\ f & 1 \\ 0 & 0 \end{pmatrix}, W_p = \frac{1}{\sqrt{1+f^2}}\begin{pmatrix} 0 & 0 \\ if & -i \\ 0 & 0 \\ i & if \end{pmatrix}, V_m = \frac{1}{\sqrt{1+f^2}}\begin{pmatrix} f & -1 \\ 0 & 0 \\ 1 & f \\ 0 & 0 \end{pmatrix}, W_m = \frac{1}{\sqrt{1+f^2}}\begin{pmatrix} 0 & 0 \\ i & -if \\ 0 & 0 \\ if & i \end{pmatrix}. \tag{S3.11}$$

The onsite green function $G = (E\mathbb{1} - M_{n'})^{-1}$ becomes

$$(\det(M_{n+1})\det(M_n) - \alpha_c^2 k^4)G = \tag{S3.12}$$
$$\begin{pmatrix} [E+n\Omega]\det(M_{n+1}) & i[\det(M_{n+1}) + \alpha_c^2 k^2] & -\alpha_c k^2[E+n\Omega] & -i\alpha_c[E+n\Omega][E+(n+1)\Omega] \\ -ik^2\det(M_{n+1}) & [E+n\Omega]\det(M_{n+1}) & i\alpha_c k^4 & -\alpha_c k[E+(n+1)\Omega] \\ -\alpha_c k^2[E+(n+1)\Omega] & -i\alpha_c[E+n\Omega][E+(n+1)\Omega] & [E+(n+1)\Omega]\det(M_n) & i[\det(M_n) + \alpha_c^2 k^2] \\ i\alpha_c k^4 & -\alpha_c k^2[E+n\Omega] & -ik^2\det(M_n) & [E+(n+1)\Omega]\det(M_n) \end{pmatrix}.$$

Collecting these elements yields the transfer matrix

$$T_{n'} = \begin{bmatrix} (W_p^\dagger G V_P \Xi)^{-1} & -(W_p^\dagger G V_P \Xi)^{-1}(W_p G V_m \Xi) \\ (W_m^\dagger G V_p \Xi)(W_p^\dagger G V_P \Xi)^{-1} & (W_m^\dagger G V_m) - (W_m^\dagger G V_p \Xi)(W_p^\dagger G V_P \Xi)^{-1}(W_p G V_m \Xi) \end{bmatrix}. \tag{S3.13}$$

By multiplying symmetric sets of this transfer matrix, one can obtain an exact analytical expression for the critical point to the desired precision.

Supplementary Note 4. MOMENTUM SHIFT BETWEEN CLASSICAL AND EFFECTIVE FLOQUET HAMILTONIAN APPROACHES

The critical momentum computed from the Floquet operator $\hat{U}_F$ and the classical PTC Hamiltonian $\tilde{H}_F$ (with higher-order terms included) coincide, while there is an overall momentum shift when using the effective Floquet Hamiltonian $\hat{H}_F^{\text{eff}}$. This shift occurs because Floquet-photonic sites with onsite energy away from $E = (\delta n_k)\Omega/2$ at $k = \Omega/2$ are intentionally dropped in the effective model (Supplementary Note 1). Specifically, using the transfer matrix method, the critical momentum computed from $\hat{H}_F^{\text{eff}}$ is $q_{c-} = \Omega/(2+\alpha_c)$ (Supplementary Note 2). We also derive an analytical expression for the classical momentum gap edge Q_{c-} with the desired accuracy up to any order in α_c (Supplementary Note 3). The difference between the inverse of these critical points is

$$\Omega/Q_{c-} - \Omega/q_{c-} = -\frac{1}{8}\alpha_c^2 - \frac{5}{64}\alpha_c^3 + \frac{271}{1536}\alpha_c^4 - \frac{7885}{36864}\alpha_c^5 + \frac{113531}{589824}\alpha_c^6 - \frac{1058321}{9437184}\alpha_c^7 \cdots. \tag{S4.1}$$

Figure 4 illustrates how these analytical solutions capture this momentum shift. It can be noted that including higher-order terms in α_c yields more precise results.

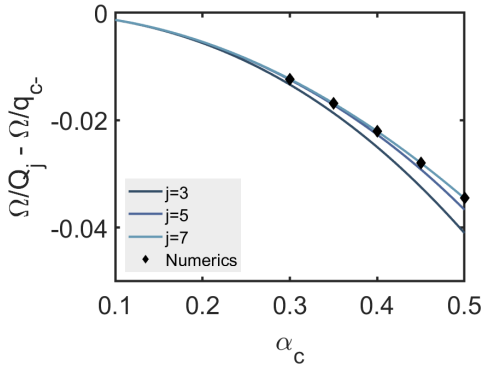

Supplementary Figure 4. Quantifying the critical-momentum shift. The symbols Q_{c-} and q_{c-} represent analytic expressions for the critical momentum derived from the classical PTC and $\hat{H}_F^{\text{eff}}$, respectively. The subscript j denotes the highest order of α_c considered. Black diamond points show the numerical difference between the inverse critical points from $\hat{U}_F$ and $\hat{H}_F^{\text{eff}}$.

Supplementary Note 5. INVERSE PARTICIPATION RATIO AND THE LOCALIZATION-TO-DELOCALIZATION TRANSITION

The inverse participation ratio (IPR) serves as a reliable indicator of the localization-to-delocalization transition, complementing the role of the localization length. Formally, the IPR is defined by

$$(\mathrm{IPR})_\psi = \frac{\sum_{n=0}^{N}\left[\psi^*(n)\,\psi(n)\right]^2}{\left(\sum_{n=0}^{N}\psi^*(n)\,\psi(n)\right)^2}, \tag{S5.1}$$

where $\psi(n) = \langle n|\psi\rangle$ is the coefficient of the wave function $|\psi\rangle$ in the orthonormal, complete basis $\{|n\rangle\}$. For a normalized state $|\psi\rangle$, the denominator simplifies to unity. The IPR reaches its maximum value of 1 if $|\psi\rangle$ occupies only one basis state $|n\rangle$. When $|\psi\rangle$ is fully delocalized in a space with size N, $\langle n|\psi\rangle \sim 1/\sqrt{N}$ and the IPR$\sim 1/N$, approaching to zero in the thermodynamic limit ($N \to \infty$). Let us specifically choose $|\psi\rangle = |\psi_m\rangle$ where $m = 0, 1, 2, \cdots$, an eigenstate of the effective Floquet Hamiltonian, with $|n\rangle$ identified as the Floquet–photon number basis state $|n, n; n\rangle$.

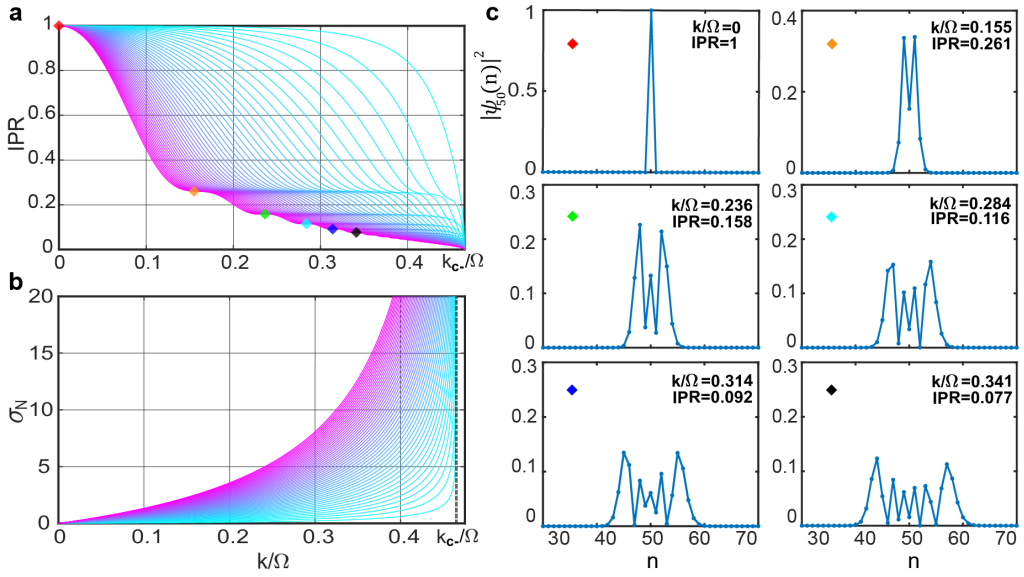

Supplementary Figure 5. Characterizing the localization of eigenstates $|\psi_m\rangle$ of $\hat{H}_F^{\text{eff}}$ (with $\delta n_k = 0, m = 0, 1, 2, \cdots 50$). (a) and (b) plot the IPR and the photon-number standard deviation for these eigenstates as functions of the photon momentum k/Ω, for eigenvalues up to the 51th. (c) The probability distribution $P(n) = |\langle n|\psi_m\rangle|^2$ of the 50th eigenstate $|\psi_{m=50}\rangle$ over the Floquet–photonic lattice, where n abbreviates the photonic states $\{|n, n; l_F = n\rangle\}$. Computations are done at $\alpha_c = 0.15$.

As $k \to k_{c-}$, the values of the IPR for each eigenstate approach zero as shown in Supplementary Fig. 5a, while the photon-number standard deviation $(\sigma_N)_{\psi_m} = \sum_{n=0}^{N}\langle\psi_m|\,\hat{N}^2\,|\psi_m\rangle - \langle\psi_m|\,\hat{N}\,|\psi_m\rangle^2$ diverges, Supplementary Fig. 5b. This indicates that the localization-to-delocalization transition occurs at the critical momentum, with all eigenstates becoming delocalized. When $k \in \mathcal{K}_{\text{band}}$ (the localized region), states with larger eigenvalues tend to spread earlier. This is consistent with the scaling of hopping terms of $\hat{H}_F^{\text{eff}}$ linear in n.

It is instructive to note that the inverse participation ratio (IPR) exhibits unusual plateaus not captured by the photon-number standard deviation σ_N. At each such plateau, the IPR ceases to decrease and instead remains nearly constant. Supplementary Figure 5c illustrates the probability distribution of the 51th eigenstate $|\psi_{m=50}\rangle$ in the Floquet-photon number basis, revealing that each new plateau emerges when the wave function acquires an additional node–antinode pair in the direction toward $n = 0$, not in the direction toward $n \to \infty$ as the IPR of $|\psi_{m=0}\rangle$ does not show any plateau. Here, the antinode corresponds to a local maximum in the probability amplitude, which the IPR can discern. In contrast, σ_N only reflects the overall spatial (photon-number) width of the wave function and thus remains insensitive to these node–antinode structures.

Supplementary Note 6. PHOTONIC ENERGY OSCILLATIONS IN THE LOCALIZED REGIME OF THE QUANTUM PTC

When a quantum state is prepared at $|\psi(t=0)\rangle = |n_k = n_{-k} = l_F = 0\rangle$, one would not expect any dynamics because it corresponds to the vacuum. However, as $k \to k_{c-}$, the localization length of eigenstates diverges and the vacuum state becomes

the superposition of eigenstates with different eigenenergies. As a result, $|\psi(t)\rangle$ shows oscillating motions for $k \in \mathcal{K}_{\text{band}}$ in the Floquet-photonic space, and so does the photonic energy $E_{\text{ph}}(t) = \langle\psi_t| \hat{H}_{\text{ph}} |\psi_t\rangle$ as shown in Fig.3b. In this section, we provide detailed analysis of the periodicity of oscillations. The vacuum state can be expanded in the eigenbasis of the effective Floquet Hamiltonian $\hat{H}_F^{\text{eff}}$ according to

$$|0\rangle = \sum_m c_m |\psi_m\rangle ,$$

where $|\psi_m\rangle$ are eigenstates labeled such that the state with the smallest photon number corresponds to $m = 0$, and the photonic energy increases sequentially with higher m.

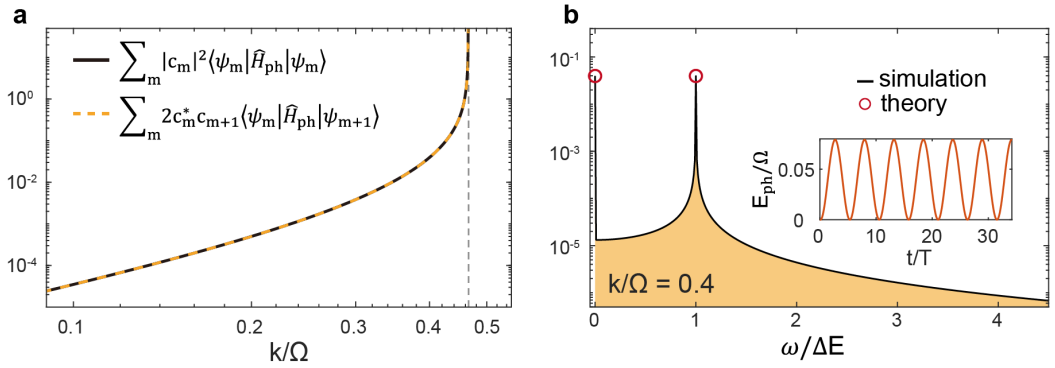

Supplementary Figure 6. (a) Amplitude of the DC component $\sum_m |c_m|^2 \langle\psi_m|\hat{H}_{\text{ph}}|\psi_m\rangle$ (solid black line) and the oscillating component $\sum_m 2c_m^* c_{m+1} \langle\psi_m|\hat{H}_{\text{ph}}|\psi_{m+1}\rangle$ (yellow dashed line) as the momentum k approaches the momentum gap edge. Here, δn_k is set to 0. Both components exhibit divergence near the edge. (b) Frequency spectrum of $E_{\text{ph}}(t)$ for $k/\Omega = 0.4$, showing a DC peak and additional peaks at $\omega/\Delta E = 1$. The black line represents simulation results, and red circles denote theoretical predictions. The inset displays the simulated time evolution of $E_{\text{ph}}(t)$, consistent with the spectrum.

The photonic energy $E_{\text{ph}}(t)$ of a system initially in the vacuum state is given by

$$\begin{aligned} E_{\text{ph}}(t) &= \langle\psi(t)| \hat{H}_{\text{ph}} |\psi(t)\rangle \\ &= \left(\sum_m c_m^* e^{iE_m t} \langle\psi_m|\right) \hat{H}_{\text{ph}} \left(\sum_{m'} c_{m'} e^{-iE_{m'} t} |\psi_{m'}\rangle\right) \\ &= \sum_{m,m'} c_m^* c_{m'} e^{i(E_m - E_{m'})t} \langle\psi_m| \hat{H}_{\text{ph}} |\psi_{m'}\rangle . \end{aligned} \tag{S6.1}$$

Since $\hat{H}_F^{\text{eff}}$ is real symmetric, its eigenstates $|\psi_m\rangle$ can be taken to have real amplitudes, making the coefficients c_m real numbers. In the thermodynamic limit for $k < k_{c-}$, the energy spacing ΔE between successive eigenenergies becomes uniform, that is, $E_m = E_0 + m\,\Delta E$. Substituting this into Eq. (S6.1), we obtain

$$E_{\text{ph}}(t) = \sum_m |c_m|^2 \langle\psi_m| \hat{H}_{\text{ph}} |\psi_m\rangle + 2 \sum_m \sum_{m'>m} c_m^* c_{m'} \langle\psi_m| \hat{H}_{\text{ph}} |\psi_{m'}\rangle \cos\left[(E_m - E_{m'})t\right]. \tag{S6.2}$$

Since $E_{m'} - E_m = (m' - m)\,\Delta E$, we introduce $\ell = m' - m$ to rewrite the oscillatory sum:

$$E_{\text{ph}}(t) = \sum_m |c_m|^2 \langle\psi_m| \hat{H}_{\text{ph}} |\psi_m\rangle + 2 \sum_{\ell=1}^{\infty} \sum_m c_m^* c_{m+\ell} \langle\psi_m| \hat{H}_{\text{ph}} |\psi_{m+\ell}\rangle \cos(\ell \Delta E t). \tag{S6.3}$$

The first term represents the time-independent average photon number (DC component), while the second term corresponds to the oscillatory components. In the localized regime, $\langle\psi_m| \hat{H}_{\text{ph}} |\psi_{m+\ell}\rangle$ decreases rapidly with increasing ℓ. As illustrated in Supplementary Fig. 6a, both the DC component ($l = 0$) and the oscillating term ($l = 1$) grow sharply near the momentum gap edge. On the other hand, for $\ell \geq 2$, the terms become negligible as shown in Supplementary Fig. 6b, leaving only the dominant frequency component corresponding to $\ell = 1$. This implies that the oscillation frequency of $E_{\text{ph}}(t)$ in the localized regime

corresponds to the energy spacing ΔE of the quantum PTC.

Supplementary Note 7. RABI DYNAMICS IN THE QUANTUM PTC WITH AN INITIALLY GROUND-STATE ATOM

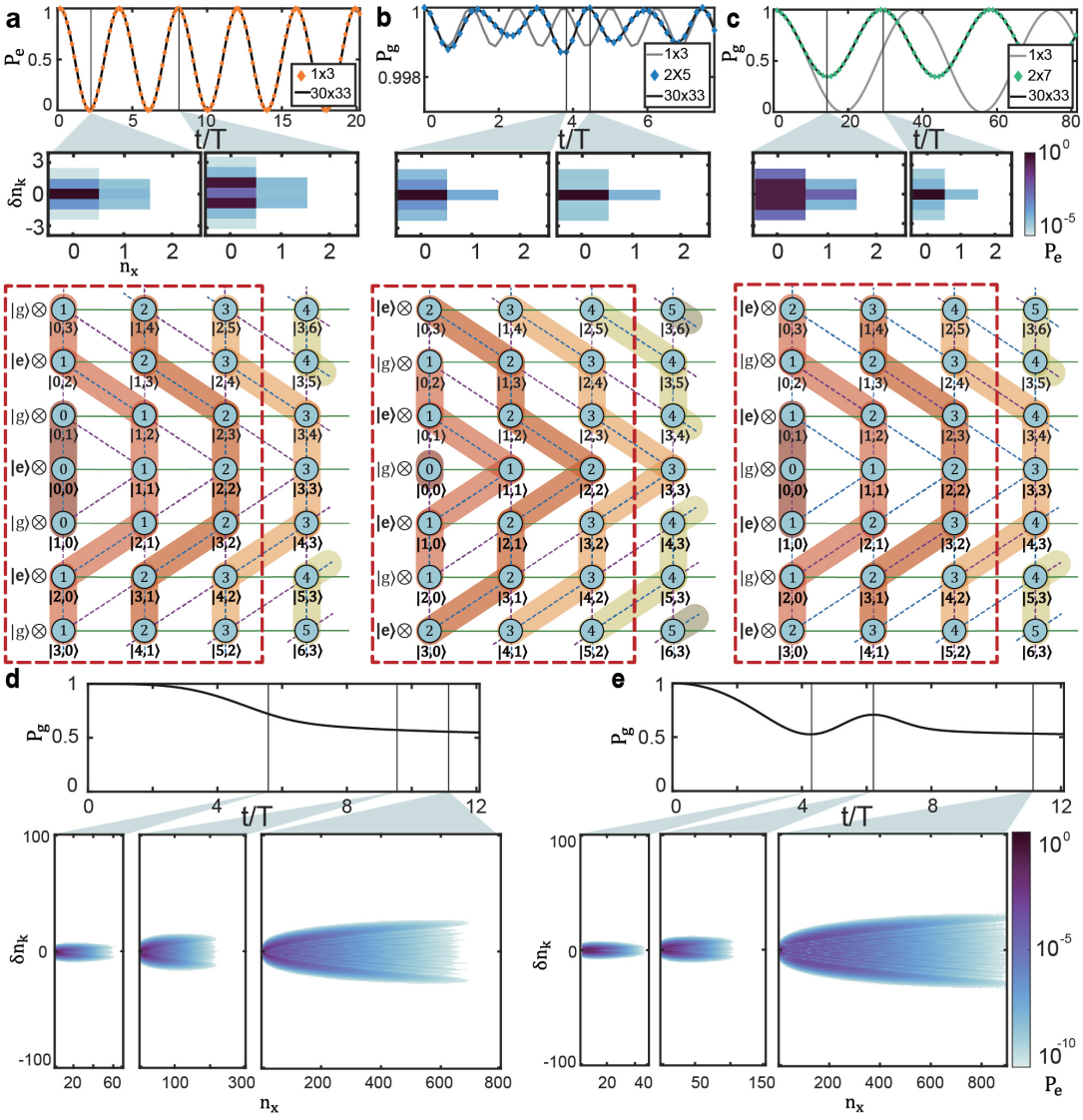

Supplementary Figure 7. Dynamics of the wave function initially prepared at $|n_k, n_{-k}; l_F\rangle = |0,0;0\rangle$ with various atomic state conditions. (a-c) The localized regime simulations are conducted under the conditions of $\alpha_c = 0.15$, $k = 0.215k_c$, and $g = 0.2$. The upper panels represent the probability of excited or ground atomic state over time with different system sizes (N_x, N_y). The lower panels are the Hilbert space most relevant for the quantum dynamics of corresponding atom-photon hybrid systems. The middle panels show the distribution of wave function in the Hilbert space (red dotted box). (a) The atomic energy spacing is set to $\Delta = k$ and an initial state is prepared in $|0,0;0\rangle \otimes |e\rangle$. (b,d) The atomic energy spacing is set to $\Delta = k$ and an initial state is prepared in $|0,0;0\rangle \otimes |g\rangle$. (c,e) The atomic energy spacing is set to $\Delta = \Omega - k$ and an initial state is prepared in $|0,0;0\rangle \otimes |g\rangle$. (d) A similar simulation is performed as (b) but $k = 1.075k_c$, $g = 0.03$ is used. (e) A similar simulation is performed as (c) but $k = 1.075k_c$, $g = 0.03$ is used. For the latter two cases, using $k \in \mathcal{K}_{\text{gap}}$, the delocalization of quantum state is observed as shown in Fig.4d, and the atomic state converges to $\rho_{\text{at}} = \frac{1}{2}(|g\rangle\langle g| + |e\rangle\langle e|)$.

The quantum Rabi model in the quantum PTC has the three independent energy scales: (i) single photon energy $\hbar ck$, (ii) the driving frequency of the permittivity Ω generating the Floquet lattice with onsite energy $-l_F\hbar\Omega$, and (iii) the energy spacing of the lowest two atomic states Δ from $\hat{H}_{\text{at}} = \frac{1}{2}(\hat{I} + \hat{\sigma}_z)\Delta$. And, there are two additional coupling strengths α_c and g, which are responsible for pair creation/annihilation of photons and the interaction between atomic states and the quantum PTC, respectively.

In the main text, we set the atomic energy $\Delta = \hbar ck$ which leads the resonant condition for $k \ll k_{c-}$ and the conventional quantum Rabi dynamics is seen (Fig.4b and Supplementary Fig. 7a). In this case, the accessible synthetic lattice sites by quantum tunneling from $|0,0;0\rangle \otimes |e\rangle$ are $|0,1;0\rangle \otimes |g\rangle$ and $|1,0;0\rangle \otimes |g\rangle$, grouped by the equipotential line around $\mathbf{n} = (0,0)$. Supplementary Figure 7a (lower panel) shows that $P_e(t)$ remains the same for choosing different system sizes: $(N_x, N_y) = (1,3)$ or $(N_x, N_y) = (30,33)$, because eigenstates are much localized on each synthetic lattice site.

When we prepare an initial quantum state at $|0,0;0\rangle \otimes |g\rangle$ the nearest synthetic lattice sites in terms of onsite potential energy is drawn in Supplementary Fig. 7b (lower panel with equipotential lines). The atomic energy spacing $\Delta = k$ is still used. For $k \ll k_{c-}$, the quantum state is locked and barely show a dynamics as reflected in $P_g(t)$. For the same initial quantum state, but $k \in \mathcal{K}_{\text{gap}}$, as shown in Supplementary Fig. 7d it shows completely different dynamics in the synthetic space by the same reason explained in the main text: the localization-to-delocalization transition also takes place in the Floquet-photonic space combined with atomic states specified in Supplementary Fig. 7b lower panel. The atomic state approaches to the half-half mixed state $\hat{\rho}_{\text{at}} = \frac{1}{2}(|g\rangle\langle g| + |e\rangle\langle e|)$ from $\hat{\rho}_{\text{at}}(t=0) = |g\rangle\langle g|$, where $\rho_{\text{at}}(t) = \text{Tr}\,[|\psi(t)\rangle\langle\psi(t)|]$ and the trace is taken over the Floquet-photonic space. The photonic energy exponentially grows over time. As a result, we reach to the claimed conclusion in the main text that irrespective of initial atomic states it converges to the half-half mixed state when $k \simeq k_{c-}$ or $k \in \mathcal{K}_{\text{gap}}$.

If we tune the atomic energy spacing $\Delta = \hbar\Omega - \hbar ck$, the landscape of equipotential lines drawn in Supplementary Fig. 7c lower panel looks similar to that of Supplementary Fig. 7a lower panel, but with an initial quantum state prepared at $|0,0;0\rangle \otimes |g\rangle$. As a result, for $k \ll k_{c-}$ it shows the oscillation similar to the conventional Rabi model. However, the $\min(P_g)$ does not reach zero (see Supplementary Fig. 7c) because of the coupling network is different from Supplementary Fig. 7a, drawn by green(α_c), blue(g), and purple($\alpha_c g$). For $k \in \mathcal{K}_{\text{gap}}$, the delocalization of eigenstates leads the growth of photonic energy and the dissipation of atom to the half-half mixed state as before. Interestingly, the different landscape of equipotential line by setting $\Delta = \hbar\Omega - \hbar ck$ is reflected in the non-monotonous behavior of $P_g(t)$ shown in Supplementary Fig 7e.

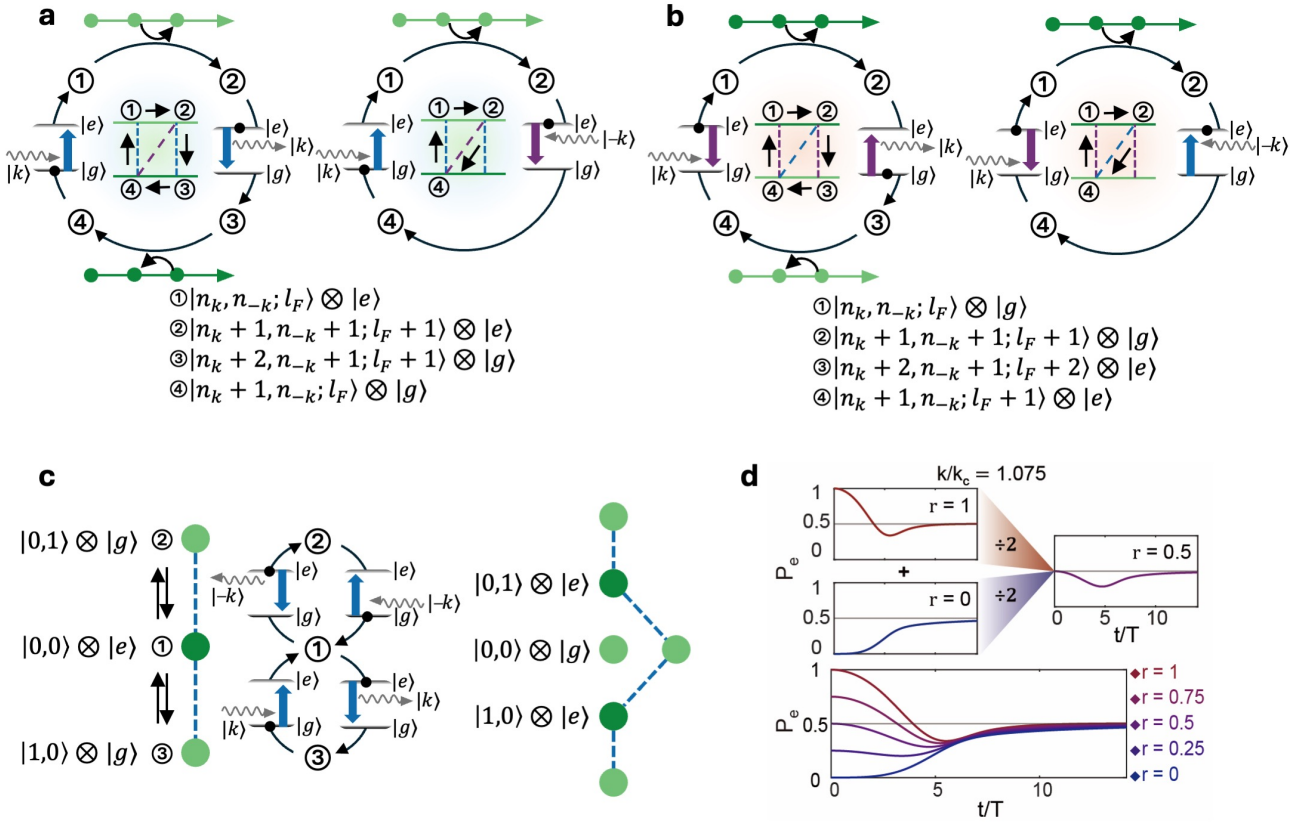

Supplementary Figure 8. Quantum transitions in the quantum PTC interacting with an atomic electric dipole. (a) The transition between four neighboring states in the 2-dimensional Hilbert space including $|0,0;0\rangle \otimes |e\rangle$. (a) The transition between four neighboring states in the 2-dimensional Hilbert space including $|0,0;0\rangle \otimes |g\rangle$. (c) (Left panel) When the permittivity is time-independent, the quantum dynamics of $|0,0\rangle \otimes |e\rangle$ is restricted to the three states showing the conventional quantum Rabi oscillation. (Right panel) For $|0,0\rangle \otimes |g\rangle$, there is no resonant transition to the nearby states and therefore it shows no quantum dynamics. (d) When an atomic state coupled to the quantum PTC at $k/k_c = 1.075$ (in the momentum gap) is initially prepared as $|\Phi\rangle_{t=0} = |0,0;0\rangle \otimes \left[\sqrt{r}|e\rangle + \sqrt{1-r}|g\rangle\right]$, where $0 \le r \le 1$, the atomic state is dissipated into the HHMS (lower panel). The upper panel explicitly shows the case at $r = 1/2$.

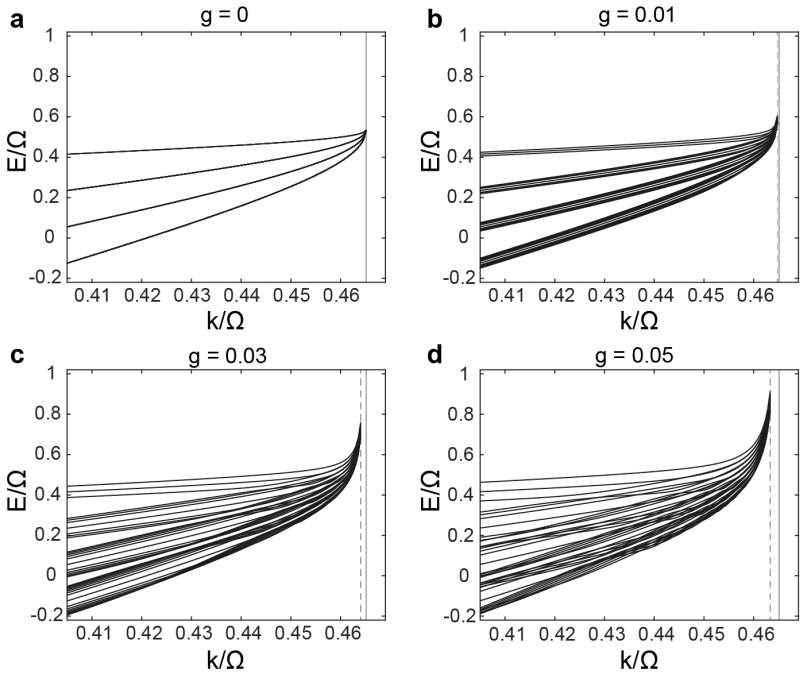

Supplementary Figure 9. Quasi-eigenenergy spectra of the atom-quantum PTC coupled system, where the atomic energy is set to $E_m^{\delta n_k=1} - E_m^{\delta n_k=0}$. (a) For $g = 0$, the quasi-eigenenergies of the one-dimensional wires with different total momenta coupled with the atomic state are degenerate. (b-d) As the coupling strength g increases, the degeneracy is lifted, causing the spectra to split. Furthermore, at larger g, the quasi-eigenenergy spectra converge toward smaller k/Ω and larger E/Ω. Panels (b–d) illustrate this progression for $g = 0.01$, $g = 0.03$, and $g = 0.05$.

Supplementary Note 8. SPECTRAL ANALYSIS AND ATOMIC POPULATION DYNAMICS IN THE ATOM–QUANTUM PTC SYSTEM

In this section, we numerically investigate how the coupling strength g alters the critical momentum k_c. We also examine the atomic population dynamics by varying the atomic energy E_{at}. To evaluate the effects of g on the system, we calculate the quasi-eigenenergy spectra for different values of g by numerically diagonalizing the total Hamiltonian, $\hat{H} = \hat{H}_F^{\text{eff}} + \hat{H}_{\text{at}} + \hat{H}_{\text{int}}$. Here, the atomic energy is set to $E_m^{\delta n_k=1} - E_m^{\delta n_k=0}$, ensuring that all one-dimensional wires with different total momenta $P = \delta n_k\, k$, when coupled to the atomic states (ground states for $\delta n_k = 1, 3, 5, \dots$ and excited states for $\delta n_k = 0, 2, 4, \dots$), share the same degenerate point (k_c, E). When $g = 0$, the quasi-eigenenergy spectrum of the atom–quantum PTC coupled system consists of degenerate bands merging at k_c, as illustrated in Supplementary Fig. 9(a), where the four lines correspond to $\delta n_k = 0, 1, 2, 3$, respectively. As g increases, these degenerate bands begin to split. Notably, near k_{c-}, initially split bands remerge, causing the critical point k_{c-} to shift to lower k, as indicated by the dotted line in Supplementary Fig. 9(b)–(d). In addition, the energy at which the spectra reconverge shifts toward higher values.

We next examine the emergent resonances and population dynamics in the atom–quantum PTC coupled system, focusing on how the atomic energy E_{at} affects the excited-state probability P_e. Concretely, we run the time evolution of a quantum state initially prepared at $|\psi(t=0)\rangle = |n_k = 0, n_{-k} = 0; l_F = 0\rangle \otimes |e\rangle$ and measure the population of excited state: $P_e(t) = \langle e|\text{Tr}\left[\hat{\rho}(t)\right]|e\rangle$ where $\hat{\rho}(t) = |\psi(t)\rangle\langle\psi(t)|$ and the trace is over the Floquet-photonic basis. As shown in Supplementary Fig. 10(a), we plot the minimum value of P_e, $\min(P_e)$, as a function of the normalized atomic energy E_{at}/Ω. In our simulations, E_{at} is varied, and the minimum P_e is extracted from the time evolution of the atomic population. A pronounced resonant dip occurs near $E_{\text{at}}/\Omega = 0.2312$. Supplementary Figure 10(b) displays the temporal evolution of P_e at this resonance, revealing both long- and short-period oscillations. The long-period oscillations originate from the transitions between $|0, 0; 0\rangle \otimes |e\rangle$ and the superposition of $|1, 2; 1\rangle \otimes |g\rangle$ and $|2, 1; 1\rangle \otimes |g\rangle$. Superimposed on these slow oscillations are short-period breathing modes, wherein the wave packet moves back and forth between adjacent lattice sites. Finally, Supplementary Fig. 10(c) depicts the onsite energies of the Floquet–photonic lattice coupled to the atomic states at $E_{\text{at}}/\Omega = 0.2312$.

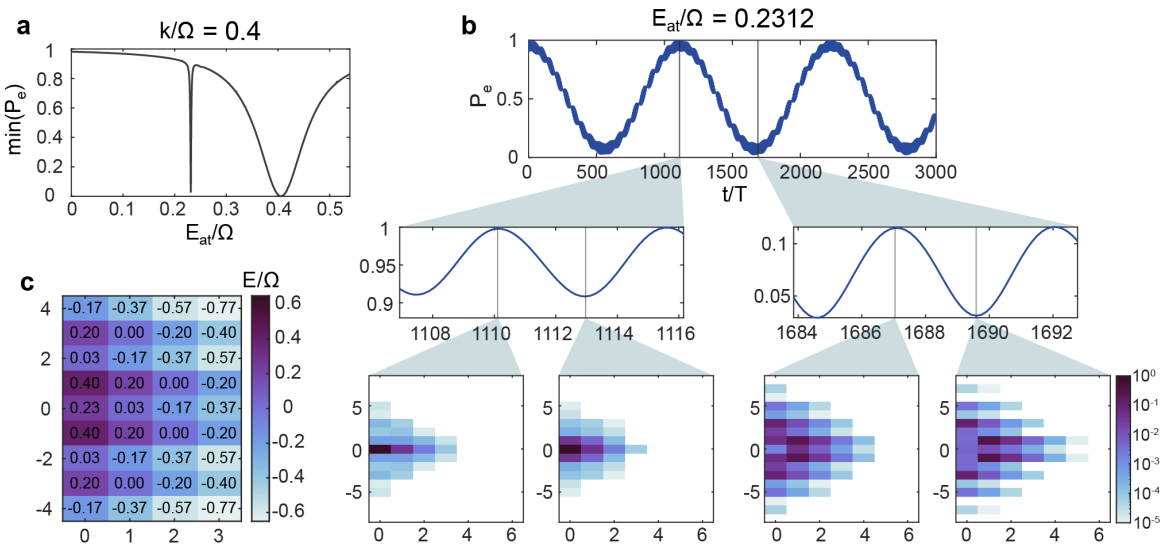

Supplementary Figure 10. (a) The minimum excited-state probability $\min(P_e)$, as a function of the atomic energy E_{at}/Ω. An additional resonant point is observed at $E_{\text{at}}/\Omega = 0.2312$ (b) The excited-state population P_e as a function of time for $E_{\text{at}}/\Omega = 0.2312$. The dynamics exhibit both long-period and short-period oscillations. The long-period oscillations correspond to transitions between $|0,0;0\rangle \otimes |e\rangle$ and superposition of the $|1,2;1\rangle \otimes |g\rangle$ and $|2,1;1\rangle \otimes |g\rangle$. The short-period oscillations involve a breathing-like motion centered around states with neighboring sites. The lower panels show $|\langle \mathbf{n}|\psi_t\rangle|^2$. (c) Onsite energies of the Floquet-photonic lattice coupled to atomic states for $E_{\text{at}}/\Omega = 0.2312$ (see Fig.4a for the corresponding base states at $\mathbf{n}$). The colormap illustrates the variation of onsite energies across the lattice sites.

Supplementary Note 9. RELATION TO THE DYNAMICAL CASIMIR EFFECT

- The quantum theory of the electromagnetic field confined by a moving boundary was first considered by Moore [11] in the Heisenberg picture. Its description in the Schrodinger picture and the effective Hamiltonian were devised in Ref. [12]: $H = \omega(t)\hat{a}^\dagger\hat{a} - i\chi_t(\hat{a}^2 - \hat{a}^{\dagger 2})$. The time-varying optical cavity setup has drawn significant attention because of photon generation by amplifying the vacuum fluctuations under the resonant condition [13, 14], $\omega_{\text{photon}} = \frac{1}{2}\omega_{\text{boundary}}$. The phenomenon is known as the *dynamical Casimir effect* (DCE). The comprehensive reviews can be found in Refs. [15, 16].

- The exponent of the total energy (photon number) growth [14] (Eq. 7.13) is given by $\langle\hat{n}\rangle = \sinh^2(\omega_0\gamma t)$. This result can be recovered from our exponent expression at $k = \frac{1}{2}\Omega$. Not only at this specific point, but also more generally, our theory tells the window of momentum in which the photons are generated from the vacuum, $k_{c\pm}$, along with the analytic expression for the exponent. Above all, we reveal the quantum mechanical nature of the momentum gap transition as the localization-to-delocalization quantum phase transition and clarify its critical behavior.

- Bridging DCE and PTC frameworks: Reference [17] is, to our knowledge, the work most closely related to the first part of our manuscript, i.e., the quantum theory of PTCs. By applying the generalized Baker–Campbell–Hausdorff formulas [18], the authors obtained an explicit expression for the exponential photon-growth rate as a function of the detuning parameter, which in our notation is $k - \frac{1}{2}\Omega$.

- The quantization of the PTC was presented in Ref. [1], and its procedure closely parallels that employed for the DCE [12]. Nevertheless, there are differences that distinguish the two: (i) Cavity-free quantization versus moving-mirror DCE: A PTC generally operates without an optical cavity, so the medium remains translationally invariant. Consequently, the counter-propagating modes $|k\rangle$ and $|-k\rangle$ are distinct but degenerate in frequency. The conserved quantity is the total momentum $P = \hbar kc(n_k - n_{-k})$, where $|n_k, n_{-k}\rangle$ denotes a Fock state. This conservation law allows us to restrict the dynamics to the subset of Fock states represented as the one-dimensional "wires" in Fig. 1 that share the same P. (ii) Expansion of the Hilbert space when atoms are added: When atomic states are coupled to photons, nearest-neighbor *wires* are coupled and the Hilbert space expands from one to two dimensions (Fig. 4). In the DCE setup, by contrast, the Hilbert space is partitioned by photon-number parity (even or odd), because pair creation and annihilation couple only photonic Fock states of the same parity. (iii) Resonant condition and focus of prior work: The primary interest in the DCE community is the generation of photons from parametrically amplified vacuum fluctuations. In the DCE literature, the

resonant condition $\omega_{\text{photon}} = \frac{1}{2}\omega_{\text{boundary}}$ is often assumed, which corresponds to $k = \frac{1}{2}\Omega$ in our work. By contrast, the PTC community has focused on the transition point where photonic states move from the band into the momentum gap. This difference arises because a PTC generally supports a continuum of momenta k, whereas a typical DCE setup involves a single resonant k.

- Novel atomic dissipation channel: In addressing the quantum dynamics of atomic states coupled to the Dynamical Casimir Effect (DCE), we have acknowledged the works of Refs. [19, 20]. However, we find that the physics described in these references does not directly align with the findings of our manuscript. Specifically, we observe a novel phenomenon: the dissipation of atomic states into a half-half mixed state, given by $\rho_{\text{at}}(t \to \infty) = \frac{1}{2}|g\rangle\langle g| + \frac{1}{2}|e\rangle\langle e|$, which occurs regardless of the initial atomic state $\rho_{\text{at}}(t = 0)$, once the eigenstates of the coupled quantum PTC become delocalized in the Floquet-photonic synthetic space. This irreversible decay is distinct from processes considered in DCE, and we believe it represents an important new contribution to the understanding of atom-photon interactions in time-varying systems. Our formalism offers a precise description of this phenomenon. As such, our work provides an ideal platform for exploring the quantum electrodynamics of PTCs, unveiling new avenues for studying non-equilibrium dynamics in quantum photonics.

Supplementary References

[1] M. Lyubarov, Y. Lumer, A. Dikopoltsev, E. Lustig, Y. Sharabi, and M. Segev, Amplified emission and lasing in photonic time crystals, Science **377**, 425 (2022).
[2] K. Ishii, Localization of eigenstates and transport phenomena in the one-dimensional disordered system, Progress of Theoretical Physics Supplement **53**, 77 (1973).
[3] A. MacKinnon and B. Kramer, The scaling theory of electrons in disordered solids: Additional numerical results, Zeitschrift für Physik B Condensed Matter **53**, 1 (1983).
[4] J. L. Pichard and G. Sarma, Finite size scaling approach to anderson localisation, Journal of Physics C: Solid State Physics **14**, L127 (1981).
[5] K. Slevin and T. Ohtsuki, Critical exponent for the quantum hall transition, Phys. Rev. B **80**, 041304 (2009).
[6] V. Dwivedi and V. Chua, Of bulk and boundaries: Generalized transfer matrices for tight-binding models, Phys. Rev. B **93**, 134304 (2016).
[7] X. Luo, T. Ohtsuki, and R. Shindou, Transfer matrix study of the anderson transition in non-hermitian systems, Phys. Rev. B **104**, 104203 (2021).
[8] Y.-C. Zhang and Y.-Y. Zhang, Lyapunov exponent, mobility edges, and critical region in the generalized aubry-andré model with an unbounded quasiperiodic potential, Phys. Rev. B **105**, 174206 (2022).
[9] Z. Xiao, K. Kawabata, X. Luo, T. Ohtsuki, and R. Shindou, Anisotropic topological anderson transitions in chiral symmetry classes, Phys. Rev. Lett. **131**, 056301 (2023).
[10] N. Wang, Z.-Q. Zhang, and C. T. Chan, Photonic floquet media with a complex time-periodic permittivity, Phys. Rev. B **98**, 085142 (2018).
[11] G. T. Moore, Quantum theory of the electromagnetic field in a variable-length one-dimensional cavity, Journal of mathematical physics **11**, 2679 (1970).
[12] C. K. Law, Effective hamiltonian for the radiation in a cavity with a moving mirror and a time-varying dielectric medium, Phys. Rev. A **49**, 433 (1994).
[13] V. V. Dodonov, A. B. Klimov, and D. E. Nikonov, Quantum phenomena in nonstationary media, Phys. Rev. A **47**, 4422 (1993).
[14] V. V. Dodonov and A. B. Klimov, Generation and detection of photons in a cavity with a resonantly oscillating boundary, Phys. Rev. A **53**, 2664 (1996).
[15] V. V. Dodonov, Current status of the dynamical casimir effect, Physica Scripta **82**, 038105 (2010).
[16] V. Dodonov, Fifty years of the dynamical casimir effect, Physics **2**, 67 (2020).
[17] R. Román-Ancheyta, I. Ramos-Prieto, A. Perez-Leija, K. Busch, and R. d. J. León-Montiel, Dynamical casimir effect in stochastic systems: Photon harvesting through noise, Phys. Rev. A **96**, 032501 (2017).
[18] M. Ban, Decomposition formulas for su(1, 1) and su(2) lie algebras and their applications in quantum optics, J. Opt. Soc. Am. B **10**, 1347 (1993).
[19] A. V. Dodonov, R. L. Nardo, R. Migliore, A. Messina, and V. V. Dodonov, Analytical and numerical analysis of the atom–field dynamics in non-stationary cavity qed, Journal of Physics B: Atomic, Molecular and Optical Physics **44**, 225502 (2011).
[20] A. V. Dodonov, Continuous intracavity monitoring of the dynamical casimir effect, Physica Scripta **87**, 038103 (2013).